Understanding variations of thermal hysteresis in barocaloric plastic crystal neopentyl glycol using correlative microscopy and calorimetry

Journal of Physics: Energy

PAPER

Understanding variations of thermal hysteresis in barocaloric plastic crystal neopentyl glycol using correlative microscopy and calorimetry

Frederic Rendell-Bhatti[1,*], **David Boldrin**[1], **Melony Dilshad**[2], **Xavier Moya**[2] **and Donald A MacLaren**[1]

[1] SUPA, School of Physics and Astronomy, University of Glasgow, Glasgow G12 8QQ, United Kingdom
[2] Department of Materials Science & Metallurgy, University of Cambridge, Cambridge CB3 0FS, United Kingdom
[*] Author to whom any correspondence should be addressed.

E-mail: fred.rendell@glasgow.ac.uk

Keywords: thermal, hysteresis, barocaloric, caloric, entropy, plastic crystal, correlative imaging

Supplementary material for this article is available online

OPEN ACCESS

RECEIVED
29 January 2024

REVISED
28 February 2024

ACCEPTED FOR PUBLICATION
2 April 2024

PUBLISHED
9 April 2024

Abstract

Plastic crystals (PCs) exhibit solid–solid order-disorder first-order phase transitions that are accompanied by large correlated thermal and volume changes. These characteristics make PCs promising barocaloric solid-state working bodies for heating and cooling applications. However, understanding the variation of transition temperatures and thermal hysteresis in PCs with cycling is critical if these materials are to replace traditional gaseous refrigerants. Here, for the archetypal barocaloric PC neopentyl glycol (NPG), we correlate microstructure obtained from scanning electron microscopy with local and total thermal changes at the phase transition from infra-red imaging and calorimetry, respectively. We outline an evolution in microstructure as NPG recrystallises during repeated thermal cycling through its solid–solid phase transition. The observed microstructural changes are correlated with spatially inhomogeneous heat transfer, yielding direct insight into the kinetics of the phase transition. Our results suggest that the interplay of these processes affects the undesirable thermal hysteresis and the nature of the kinetic steady-state microstructures that are stabilised during cycling between the ordered and disordered phases. These observations have implications for using NPG and other PCs as technologically relevant barocaloric materials and suggest ways in which the hysteresis in these types of materials may be modified.

1. Introduction

Plastic crystals (PCs) are emerging as highly promising solid-state working bodies for use in sustainable heating and cooling applications [1–3]. Notably, the potential of PCs as environmentally friendly refrigerants was demonstrated through the recent discovery of the colossal barocaloric (BC) effect in neopentyl glycol (NPG) [4–6]. NPG exhibits a solid–solid (S–S) first-order phase transition (FOPT) between PC and ordered crystal (OC) phases. The associated entropy change is comparable in magnitude to that exploited in traditional fluid refrigerants (e.g. R134a) and an advantage of PC BC materials is that they are less volatile and do not have the high global warming potential of traditional refrigerants. This finding was a significant step towards the implementation of solid BC materials as technologically relevant refrigerants for heating and cooling applications [7–9]. In PCs, the BC effect arises from the entropy change associated with the ordering of molecules at the FOPT, which can be driven by pressure [10]. However, during thermal cycling many PCs display significant supercooling effects, manifested as thermal hysteresis, so that the heat absorption and rejection processes occur at significantly different temperatures on the heating leg and cooling leg [11]. This hysteresis is undesirable in BC applications as it increases the operational pressures required to leverage the large reversible entropy changes that occur during pressure-driven BC transitions [12, 13]. Furthermore, since supercooling can be explained as a nucleation-driven process, the FOPT temperature is often subject to

substantial variability [14, 15]. These aspects may limit the efficacy of PCs as BC refrigerants in a working device, where they will need to be cycled continuously and at low pressures [16]. Another important aspect of PCs is the fact that accompanying the FOPT there is a significant change in plasticity of the material, through liberation of orientational degrees of freedom. This suggests that microstructure and physical properties may change between successive heating and cooling cycles. Understanding supercooling behaviour and how it correlates with microstructural variations is therefore crucial for commercialising solid-state BC materials.

A significant effort has been undertaken in recent years to synthesise and understand a variety of promising BC PCs [17–22]. NPG is perhaps the best studied material, because of its colossal BC effect. Under atmospheric conditions, NPG exists in an OC phase, where its molecules are fixed into a monoclinic ($P2_1/n$ space group) crystal structure. Upon heating above $T_0 = 314$ K, hydrogen bonds between NPG molecules are broken, and the NPG undergoes a FOPT to the disordered PC phase. This results in a change of crystal structure to face-centred cubic ($Fm\text{-}3m$ space group) with an accompanied volume change of 5% [5]. Upon cooling, or the application of pressure, NPG transitions back into the OC phase. However, this does not occur at the equilibrium transition temperature, T_0, but at a lower temperature, T_{SC}. The lag is due to the phenomenon of supercooling, where NPG remains in the PC phase until a nucleation event triggers the phase transition at the supercooling temperature. Such supercooling behaviour is responsible for a thermal hysteresis (δT_{hys}) in thermally driven systems and a pressure hysteresis (δp_{hys}) in pressure driven systems. Thus, in thermally driven systems the equilibrium transition and supercooling temperatures are related through $T_0 = T_{SC} + \delta T_{hys}$.

Structural studies are usually complemented by differential scanning calorimetry (DSC) data, in order to determine the temperatures of heat absorption and rejection. Together with diffractive techniques, DSC is vital for obtaining bulk information pertaining to the S–S FOPTs in these materials. However, such bulk studies can overlook the heterogenous nature of nucleation processes, which can initiate at defects or other microstructural features. Supercooling in PCs is often a stochastic, nucleation-driven process, so that the microstructure, consequent plasticity and S–S recrystallisation temperatures may vary between successive cycles [14]. This is of particular importance in the context of BC PCs, where materials are subject to repeated compression-decompression cycles. Variation in microstructure through cycling may become significant. The aim of this work is to implement imaging techniques that can directly probe the mechanisms of phase transition nucleation, propagation, and their impact on the resulting microstructure, which are difficult to detect using bulk techniques.

We have correlated calorimetric measurements of NPG with spatially resolved observations using environmental scanning electron microscopy (ESEM) and infra-red (IR) imaging. We outline an evolution in the NPG microstructure as it undergoes S–S recrystallisation during the FOPT through repeated thermal cycling. Our results suggest that the S–S recrystallisation consists of a fast process, on a timescale of the cooling rate (minutes in the present case), and a slower process, occurring on a timescale of hours. The final crystal habit adopted by the low temperature phase is shown to align with the directions of spatially inhomogeneous heat transfer, revealed by IR imaging. We track the nucleation and subsequent propagation fronts of S–S recrystallisation throughout NPG samples, correlating our observations with features in DSC data. Our results provide insight into the supercooling behaviour and the nature of the kinetic steady-state microstructures that are stabilised during cycling. We observe a correlation between supercooling behaviour and S–S recrystallisation, where reduced supercooling in virgin cycles converges to the expected behaviour after thermal cycling. This provides valuable insight into the phenomenon of thermal hysteresis, which is of great importance in PCs for a variety of applications. We propose that variations in the S–S recrystallisation are likely to result in variations in the mechanical properties of the material during thermal cycling, and thereby affect the measured BC effect. Finally, our results demonstrate that a robust methodology is required to distinguish virgin effects from stochastic, nucleation-driven variations, and the workflow that we present will be relevant to the study of FOPTs across a wide range of orientationally disordered materials.

2. Results and discussion

Figure 1 shows an ambient pressure DSC plot for an NPG pellet (see methods section for details). It depicts the measured heat-transfer rate over ten successive cycles. On heating (red curves) the NPG behaved very reproducibly ($T_0 = 314.5 \pm 0.1$ K). In contrast, the cooling (blue) curves do not all overlap, indicating significant variation in supercooling. The variation in onset temperature for both heating and cooling is illustrated in the inset plot. Cycle 1, where $T_{SC}(1) = 303.5$ K, represents the initial behaviour of the NPG after it has been pelletised and is an outlier when compared to all subsequent cooling cycles. The remaining nine cycles exhibit a random distribution of supercooling temperatures around a mean of $T_{SC}(2{:}10) = 300.2 \pm 0.2$ K, as represented by the dashed line in the inset plot. The mean supercooling temperature agrees very well with previous measurements of thermal hysteresis in NPG [23–26]. Since we have defined the

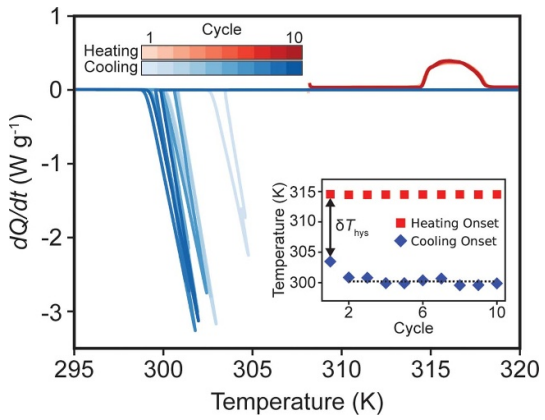

Figure 1. NPG thermal behaviour obtained using ambient pressure DSC. Sequential DSC curves of NPG through ten heating and cooling cycles, demonstrating significant supercooling effects. The variation in cooling transitions is displayed as both a 'virgin effect' associated with cycle 1 and stochastic variations in cycles 2–10. The inset plot provides the onset temperatures for each DSC curve and demonstrates the hysteresis (δT_{hys}) arising from supercooling. Positive dQ/dT here corresponds to endothermic effects and the scanning rate was 0.5 K min^{-1}.

hysteresis as $\delta T_{\mathrm{hys}} = T_{0\_}T_{\mathrm{SC}}$, the initial cycle represents a hysteresis reduction of about 23% as compared to subsequent cycles. The origin of this 'virgin effect' is difficult to determine using calorimetry alone. It should be noted that some random variation in T_{SC} is expected, since the process is driven by nucleation events that are ultimately stochastic in nature [27]. However, the systematic change observed from $T_{\mathrm{SC}}(1)$ to $T_{\mathrm{SC}}(2{:}10)$ is outwith the variation of $T_{\mathrm{SC}}(2{:}10)$ and thus requires further study into the mechanistic differences between the cycles.

To investigate the S–S recrystallisation processes in NPG, a pelletised sample was imaged before and after thermal cycling using ESEM (see Methods for details). Environmental SEM was necessary to limit the electron-beam induced sublimation of NPG at the low pressures required for traditional SEM imaging. Figure 2(a) shows a secondary electron ESEM image of the NPG sample as synthesised, taken at 263 K in the OC phase. The observed microstructure is dominated by flakes or bundles of needle-like crystallites, typically several hundred micrometres long and tens of micrometres wide. This random distribution of crystallites with localised directionality is highlighted by the inset fast Fourier transform (FFT). Discrete radial bands are observed and derive from the ordering within crystallite bundles, but there is no strong azimuthal variation in the FFT intensity, which indicates that the bundles are not all aligned in a preferential direction. A lamellar crystal structure is consistent with the flaky visual appearance of the as-purchased material and the layered molecular alignment within the OC monoclinic phase, as commented elsewhere [28]. The needle-like texture within each crystallite may derive from the slow component of S–S recrystallisation, as discussed below.

The as-prepared NPG surface (figure 2(a)) contrasts with that of figure 2(b), which shows the surface of NPG imaged at 263 K, after it has been thermally cycled between 290 K and 330 K and allowed to rest in the OC phase for 30 min at 298 K. There is a significant change in the microstructure, whereby none of the original features and crystallites are present and the sample appears more isotropic. This is confirmed by the inset FFT, which now lacks the radial bands of the as-prepared case. The most drastic change in microstructure occurs within a period of 24 h after the thermal cycling, as shown in figure 2(c). Here, both the real-space and FFT images highlight the re-emergence of a needle-like, directional microstructure, now without any obvious platelets or bundles. Furthermore, in contrast to figure 2(a), this directionality is now across the field of view, with needles aligning diagonally in the image, which produces a double cone of intensity in the FFT. This confirms that the process of thermal cycling, far below the melting temperature of NPG (403 K), causes two subsequent S–S recrystallisation processes to occur within the NPG sample. These observations demonstrate a significant variation in the OC phase of NPG microstructure during the initial thermal cycle, providing a possible explanation for the observed virgin effect in the DSC data (see figure 1). We propose that the greater structural heterogeneity observed in the OC phase of NPG in figure 2(a) is also reflected in the microstructure of the PC phase (which we cannot image under vacuum directly). Such heterogeneity would then account for the more rapid emergence of nucleation points, making nucleation of the PC-OC phase transition faster, and thereby reducing thermal hysteresis [29]. Perhaps the structural heterogeneity leads to a less isotropic strain distribution in the cooling PC material, with local extrema acting as nucleation sites and thereby reducing the supercooling effect of the virgin cycle(s). It is also interesting to note that the main exothermic process detected by DSC relates to the fast S–S recrystallisation process rather than the formation of larger crystals that are observed after 24 h. Heat output during this slow S–S

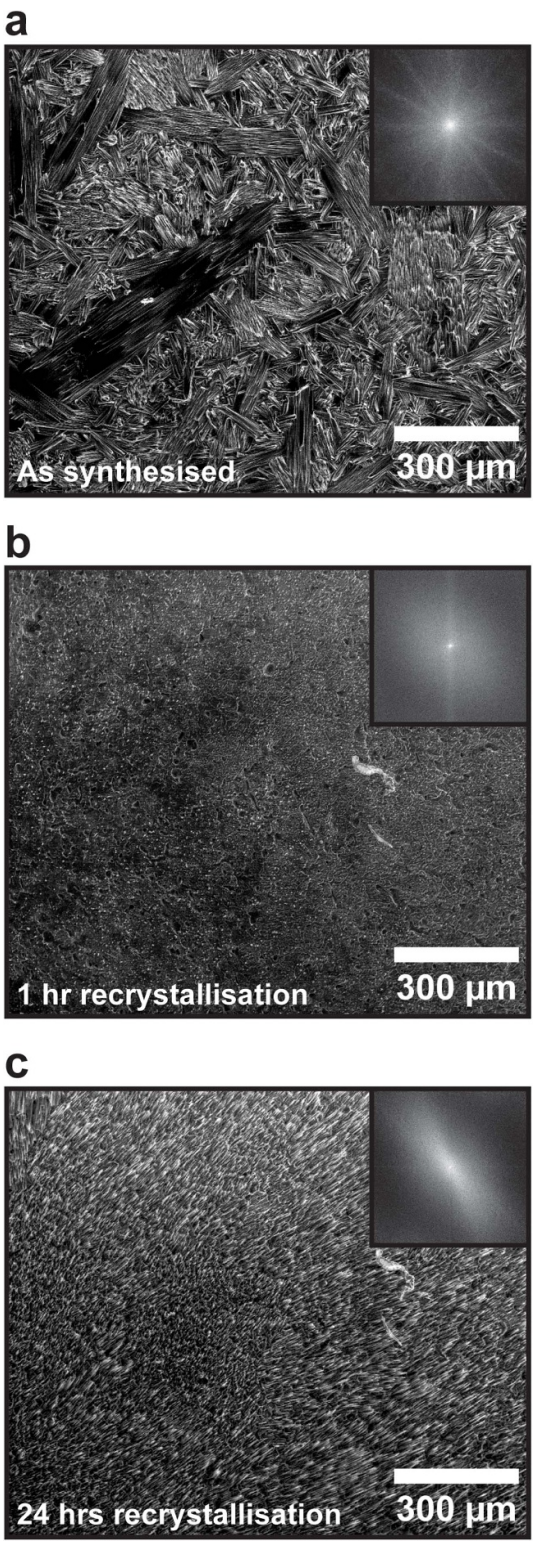

Figure 2. SEM images of the NPG surface, demonstrating S-S recrystallisation processes after thermal cycling. NPG pellet sample (a) as prepared, (b) 1 h after thermal cycling and (c) 24 h after thermal cycling. Inset FFT in each image highlights microstructure directionality present in (a) and (c), and lack of directionality in (b). Images obtained at 263 K.

recrystallisation stage would be difficult to detect and is not relevant to the use of NPG in heat-pumping systems that would be operating continuously.

Further investigation into the origin of the directionality and preferred orientations in the recrystallised microstructure was performed by correlating ESEM with IR imaging. An advantage of the latter is that it is performed under atmospheric conditions, so that both OC and PC phases can be imaged directly. A single sample of NPG was sequentially imaged using ESEM and IR to systematically characterise the sample before, during and after successive thermal cycles (see methods for details). Figure 3 demonstrates this process for

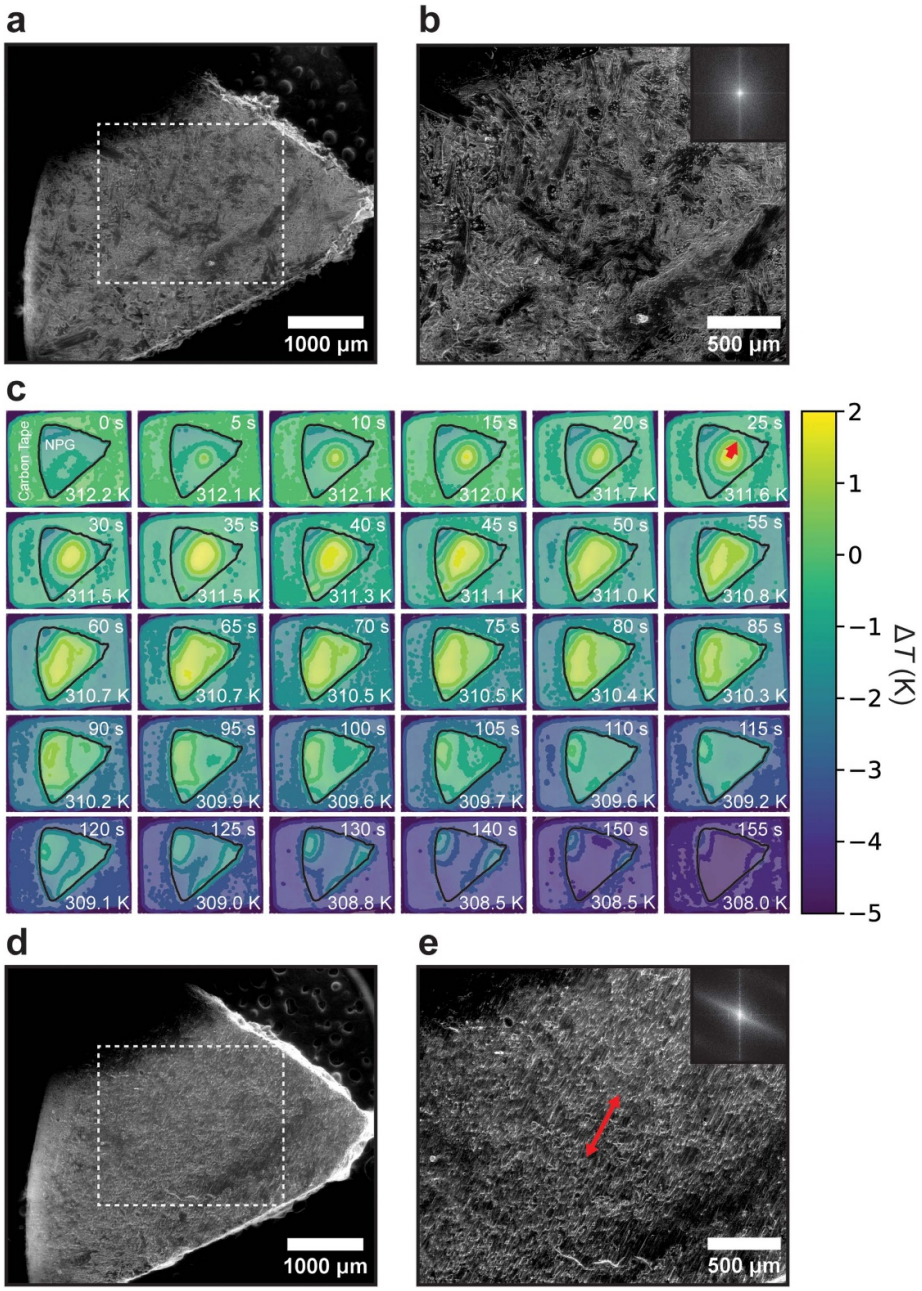

Figure 3. Correlated ESEM/IR imaging for NPG for the first heating and cooling cycle. (a), (b), ESEM secondary electron images of the NPG sample prior to thermal cycling. The area enclosed by the dashed rectangle is shown at higher magnification in (b). The inset FFT in (b) shows lack of long-range directionality. (c) A sequence of IR images, where the colour indicates the temperature relative to the heating plate temperature of the first frame ($t = 0$ s). The NPG pellet is enclosed by the black line, and the area surrounding this region is carbon tape covering the heating plate. Temperature of the heating plate is given in the bottom right of each image. (d), (e), SEM secondary electron images of the NPG sample 24 h after the first heating and cooling cycle. The area enclosed by the dashed rectangle is shown at higher magnification in (e). The inset FFT in (e) highlights an emergent long-range directionality, corresponding to the real-space direction indicated by the red arrows in (e) and (c). All ESEM images obtained at 263 K.

cycle 1, where figures 3(a) and (b) are ESEM images of the as-prepared sample and figures 3(d) and (e) show the sample 24 h after thermal cycling, to allow for the slow S–S recrystallisation process to occur. Figures 3(b) and (e) and their inset FFTs are magnified images of the dotted white box regions in figures 3(a) and (d). Again, by inspecting both the real-space images and the associated FFTs, it is clear that the S–S recrystallisation process has resulted in a drastic change in microstructure. The red arrow in figure 3(e) was generated using the sharp band of intensity in the FFT, representing the dominant axis of directionality in the sample. Figure 3(c) depicts the sample as it is cooled from 310 K at 2 K min^{-1}, through the PC-OC phase transition using IR imaging. These snapshots are each separated by a time of 5 s, and the full transition occurred over approximately 155 s. The colour bar represents the difference in temperature as compared to the heating plate temperature in the $t = 0$ s frame. The phase transition proceeds first through the emergence

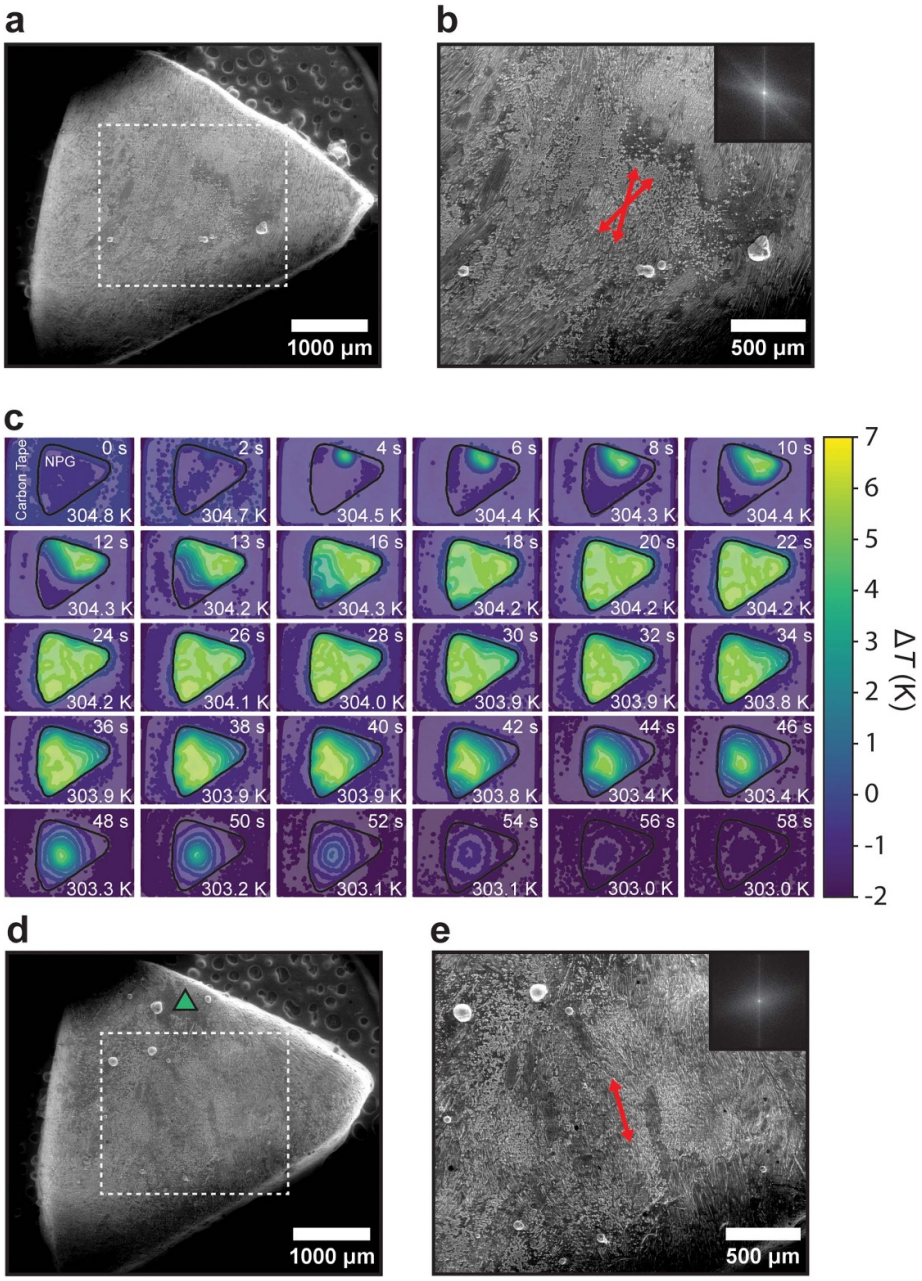

Figure 4. Correlated ESEM/IR imaging for NPG for the third heating and cooling cycle. (a), (b), SEM secondary electron images of the NPG sample after two heating and cooling cycles. The area enclosed by the dashed rectangle is shown at higher magnification in (b). The inset FFT in (b) shows two dominant directionalities, given by the red arrows. (c) A sequence of IR images, where the colour indicates the temperature relative to the heating plate temperature of the first frame ($t = 0$ s). The NPG pellet is enclosed by the black line, and the area surrounding this region is carbon tape covering the heating plate. Temperature of the heating plate is given in the bottom right of each image. (d), (e) ESEM secondary electron images of the NPG sample 24 h after heating and subsequent cooling. The area enclosed by the dashed rectangle is shown at higher magnification in (e). The inset FFT shows that microstructural directionality has changed and is almost orthogonal to that shown in (b). The green triangle in (d) indicates the location of the initial nucleation event. All ESEM images obtained at 263 K.

of a nucleation event at $t = 5$ s, followed by the radial outwards propagation from this point at an approximate surface speed of 40 μm s^{-1}. Inspecting the frames between $t = 5$ s and $t = 25$ s, the dominant direction of propagation (given by the red arrow at $t = 25$ s) closely matches the microstructure directionality, as previously determined by the FFT in figure 3(e). This suggests that the direction of the exothermic PC-OC phase transition front, as it sweeps through the sample, ultimately influences the final microstructure.

The process described above was repeated in a succession of heating and cooling cycles, and the images for cycle 3 are presented in figure 4. In this case, the original NPG pellet has been cycled twice in figures 4(a) and (b) and three times in figures 4(d) and (e). The unpredictable nature of the supercooling transition is apparent because in this cycle, the nucleation point is evident on the upper edge of the pellet (see the IR

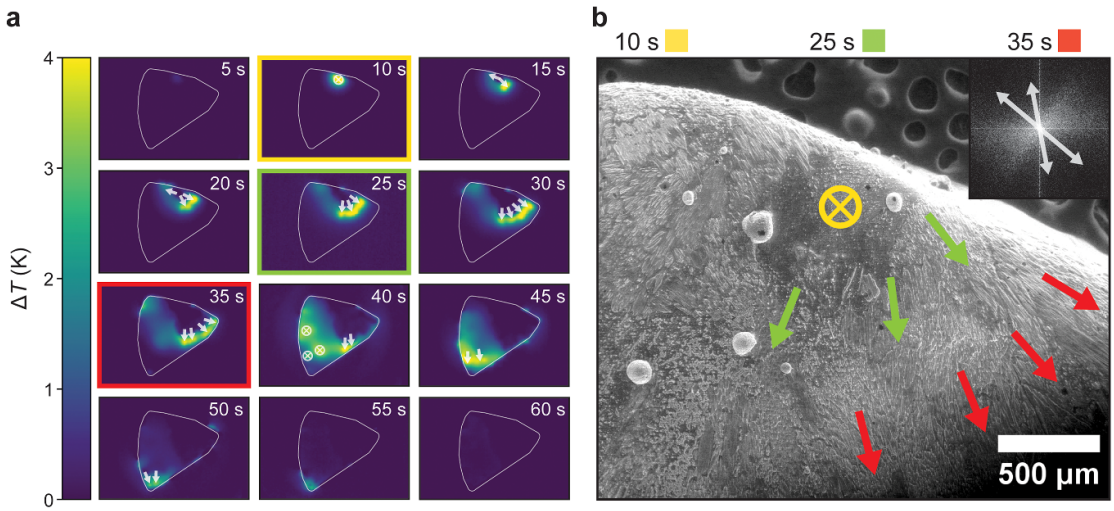

Figure 5. Correlation between IR difference images and the recrystallised microstructure imaged using SEM. (a), IR difference images, obtained from calculating the difference between frame $n + 1$ and frame n. The colour bar is such that only regions that have increased in temperature in sequential frames are evident. Crosses and arrows demonstrate the nucleation and phase transition fronts respectively. (b) SEM secondary electron image after 24 h of the phase transition shown in (a). Coloured arrow annotations correspond to the same-coloured frames in (a). The inset FFT highlights two dominant directionalities, with real-space directions given by the white arrows. The FFT was calculated using the bottom right corner of the image, localised around the coloured arrows. The ESEM image was obtained at 263 K.

image at 4 s in figure 4(c)), distinct from the nucleation point shown in figure 3(c). In this sense, we are unable to use geometric or microstructural features to predict nucleation locations. Comparison of the ESEM images in figures 4(b) and (e) indicate that although the microstructure has changed upon thermal cycling, its characteristics are similar. The FFTs show weak ordering (and small crystallites) in both cases, with the axis of directionality changing, which would be consistent with a change in the nucleation point in successive cycles. This similarity in structure is consistent with the similarity of heat output measured with DSC (figure 1). In other words, the variation in microstructure is consistent with the variation in supercooling behaviour. We also note here the appearance of small globular features on the surface of the sample, which appear to be almost-spherical crystallites of NPG (see supplementary figure 1). These features disappear during thermal cycling and reappear during the 24 h S–S recrystallisation period (see figures 4(b) and (e)). No clear correlation between their location and the phase transition process was found, and it is likely that they formed randomly through surface-nucleation processes during the S–S recrystallisation period. Inspecting the IR imaging snapshots in figure 4(c), the phase transition during cycle 3 occurs over a much shorter time (58 s) than cycle 1 (155 s), with the calculated phase transition propagation speed being 190 μm s^{-1}, five times faster than for cycle 1. As the same amount of heat is expelled, but in a shorter time, the IR images show a greater maximum temperature reached in cycle 3 compared to cycle 1, which accounts for the narrower peaks in DSC data after the first cycle. This acts to obscure any further nucleation events that may have occurred after the initial event (at $t = 4$ s). To overcome this, difference IR images were obtained by calculating the temperature difference between each successive frame. These difference images are presented in figure 5(a), where the colour bar has a lower cutoff of zero, such that only pixels that increased in temperature relative to the previous frame are coloured. Furthermore, since the initial nucleation event location (represented by the green triangle in figure 4(d)) occurred just outside the magnified region in figures 4(e), a second magnified ESEM image localised around the nucleation region was obtained, as shown in figure 5(b).

The difference IR frames in figure 5(a) show more clearly both the nucleation events (white circled crosses) and subsequent phase transition propagation directions (white arrows). By using the IR images in this way, it is possible to track the phase transition as it moves through the material and to observe new wavefronts formed by successive nucleation events (e.g. see $t = 40$ s). The microstructure around the initial nucleation region is shown clearly in figure 5(b), where both short- and long-range directionality is present. The microstructure around this nucleation region (annotated by the yellow circled cross) is more homogenous and anisotropic than the surrounding regions. This may be due to nucleation within the sample, so that crystal growth here is normal to the surface. Subsequent S–S recrystallisation within the surface plane is represented by the green and red arrows in figure 5(b), which are drawn parallel to the local microstructure directionality. These directions derive from the inset FFT (taken from a smaller region

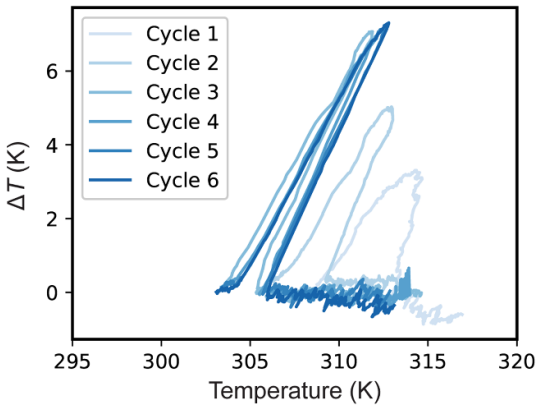

Figure 6. Thermally driven ΔT of NPG using IR imaging over multiple cycles. Here the temperature difference between the sample and heating plate (ΔT) is shown as a function of the heating plate temperature. Both the virgin (cycles 1 and 2) and the stochastic (cycles 3–6) variations are observed.

around the green and red arrows), where the annotated white arrows are orthogonal to the two dominant intensity lobes, corresponding to the associated real-space directions. The directionality specified by the green and red arrows has been correlated to the IR difference frames with the same-coloured borders. This confirms how the spatio-temporal details of heat transfer throughout the phase transition influences the final microstructure.

Next, we directly compare the data obtained from IR imaging with that obtained from DSC (figure 1). In figure 6, the increase in the average temperature of the NPG pellet during the FOPT is plotted as a function of the heating plate temperature, obtained from the IR measurement of the carbon tape. It should be noted that there is a difference in absolute measured transition temperatures (IR compared to DSC), which is likely due to a temperature offset in the IR data due to relatively poor thermal contact between the heating plate and the top surface of the carbon tape. Furthermore, the cooling rate during the IR imaging was 2 K min^{-1}, compared to 0.5 K min^{-1} in the DSC experiment. However, these data still show a remarkable likeness to the DSC data in figure 1, where both the virgin effect behaviour (cycles 1 and 2) and the expected stochastic behaviour associated with homogenous nucleation (cycles 3–6) are present. In this case, however, it takes two cycles before the representative behaviour is reached. The faster cooling rate likely explains this observation, as the material spends less time at elevated temperatures during IR imaging and may not have fully equilibrated. We suggest that it takes some time to anneal the microstructure during thermal cycling, and for trace of the as-prepared microstructure (figure 3(b)) to be lost, in favour of an equilibrium microstructure distribution (represented by figures 4(b) and (e)). The microstructures associated with figures 3(b) and (e) can be seen as extremes, where figure 3(b) shows many randomly oriented crystallites with short-range order and figure 3(e) consists of ordered crystallites with long-range order. The microstructures obtained after cycle 2 represent intermediates between these two extremes. Finally, we note that the fast S–S recrystallisation process may be influenced by the cooling rate and the observations made here are for similar, relatively slow rates (0.5 and 2.0 K min^{-1}). In a pressure-driven heating/cooling system, the cycling rate may be significantly faster, such that a steady-state microstructure is never achieved for either solid phase, and the virgin effect may persist for many cycles. Future studies into S–S recrystallization processes of PCs at higher cooling rates and/or pressure driven systems will be valuable.

3. Conclusions

Through a combination of DSC, ESEM and IR imaging in a correlative study we have provided an explanation for the virgin effect variation in supercooling behaviour observed in the PC NPG. ESEM imaging revealed a clear variation in microstructure during the initial thermal cycles, mirroring the thermal variation observed using DSC and IR imaging. Since successive thermal cycling acts to anneal the as-prepared microstructure, representative thermal behaviour is reached once an equilibrium microstructure is obtained. This highlights the importance of preliminary cycling of PCs, to ensure representative behaviour is measured. The heterogeneous microstructure of the as-prepared sample provides an explanation for the reduced hysteresis observed in the virgin effect, until successive thermal cycles fully anneal this microstructure. This further suggests that methods of influencing S–S recrystallisation processes may result in different FOPT behaviour on cooling. It is important to note that we have presented an example of thermal hysteresis variation that is independent of sample geometry or the presence of additional inclusions,

which have been discussed in the recent NPG literature [14, 30–32]. We have additionally demonstrated the strength of combining multiple imaging techniques in the study of BC materials, specifically in the ability to link microstructure with spatio-temporal thermal processes during their FOPTs. This analysis directly complements traditional bulk calorimetric methods and allows for probing of mechanistic details that are not accessible using DSC. The application of these methods to other BC materials, particularly technologically promising PCs, will aid in the understanding of their non-trivial supercooling behaviour.

4. Methods

Powder samples of NPG (99% purity) were purchased from Sigma-Aldrich and used as received. Pellets of 13 mm diameter and 0.8 mm thickness were pressed using a uniaxial press and a pressure of 10 MPa. These pellets were cut into appropriate sizes for each experiment. Samples were stored in sealed vials under ambient pressure and temperature between measurements. DSC data were obtained using a TA instruments DSC 250 at a ramp rate of 0.5 K min^{-1}. Secondary electron images were obtained using an FEI Quanta 200F environmental SEM instrument at a pressure of 130 Pa and a temperature of 263 K, via cooling using a Peltier stage; this environment was chosen to reduce the beam-induced sublimation of NPG. IR imaging was performed using an Optris PI640 IR microscope camera, with the samples mounted to the ESEM Peltier stage. The NPG sample was affixed to the stage using carbon tape and the emissivity of the NPG sample was adjusted in the data acquisition software until the measured temperature for NPG matched that of the strip of carbon tape that was in direct contact with the Peltier stage. Thus, for IR imaging, all reported temperatures are relative and not absolute. Heating and cooling were performed at a rate of 2 K min^{-1} during IR imaging. Correlative imaging was performed on the same sample of NPG, after pelletisation, and the following describes a single correlative imaging cycle. The sample was first imaged in the ESEM at 130 Pa and 263 K, which was immediately followed by IR imaging at ambient pressures on cooling from 330 to 290 K. The sample was then left in a sealed container under ambient pressure and temperature for 24 h before being imaged in the ESEM again at 130 Pa and 263 K.

Data availability statement

All data that support the findings of this study are included within the article (and any supplementary files).

Acknowledgments

This work was financially supported by an EPSRC Grant (EP/V042262/1). The authors would like to thank Liene Spruzeniece for her technical support.

Author contributions

F R B performed material synthesis, data acquisition, data analysis and prepared the manuscript. D B assisted with data acquisition, data analysis, and drafting the manuscript. M D and X M assisted with data analysis and the manuscript. F R B, D B, X M and D M were responsible for conception and design of the work. D M supervised the work, assisted with data analysis and drafting the manuscript.

ORCID iDs

Frederic Rendell-Bhatti https://orcid.org/0000-0002-3470-786X
David Boldrin https://orcid.org/0000-0003-3833-8341

References

[1] Moya X, Kar-Narayan S and Mathur N D 2014 Caloric materials near ferroic phase transitions *Nat. Mater.* **13** 439–50
[2] Moya X and Mathur N D 2020 Caloric materials for cooling and heating *Science* **370** 797–803
[3] Lloveras P and Tamarit J L 2021 Advances and obstacles in pressure-driven solid-state cooling: a review of barocaloric materials *MRS Energy Sustain.* **8** 3–15
[4] Moya X, Avramenko A, Manosa L, Tamarit J L and LLoveras P 2017 *Use of barocaloric materials and barocaloric devices* PCT/EP2017/076203
[5] Lloveras P *et al* 2019 Colossal barocaloric effects near room temperature in plastic crystals of neopentylglycol *Nat. Commun.* **10** 1–7
[6] Li B *et al* 2019 Colossal barocaloric effects in plastic crystals *Nature* **567** 506–10
[7] Kitanovski A, Plaznik U, Tomc U and Poredoš A 2015 Present and future caloric refrigeration and heat-pump technologies *Int. J. Refrig.* **57** 288–98

[8] Cirillo L, Greco A and Masselli C 2023 The application of barocaloric solid-state cooling in the cold food chain for carbon footprint reduction *Energies* **16** 6436
[9] Schipper J, Bach D, Mönch S, Molin C, Gebhardt S, Wöllenstein J, Schäfer-Welsen O, Vogel C, Langebach R and Bartholomé K 2023 On the efficiency of caloric materials in direct comparison with exergetic grades of compressors *J. Phys. Energy* **5** 045002
[10] Li F B, Li M, Xu X, Yang Z C, Xu H, Jia C K, Li K, He J, Li B and Wang H 2020 Understanding colossal barocaloric effects in plastic crystals *Nat. Commun.* **11** 1–8
[11] Boldrin D 2021 Fantastic barocalorics and where to find them *Appl. Phys. Lett.* **118** 170502
[12] Hess T, Maier L M, Bachmann N, Corhan P, Schäfer-Welsen O, Wöllenstein J and Bartholomé K 2020 Thermal hysteresis and its impact on the efficiency of first-order caloric materials *J. Appl. Phys.* **127** 7
[13] Cirillo L, Greco A and Masselli C 2022 Cooling through barocaloric effect: a review of the state of the art up to 2022 *Therm. Sci. Eng. Prog.* **33** 101380
[14] Lilley D, Lau J, Dames C, Kaur S and Prasher R 2021 Impact of size and thermal gradient on supercooling of phase change materials for thermal energy storage *Appl. Energy* **290** 116635
[15] Shamseddine I, Pennec F, Biwole P and Fardoun F 2022 Supercooling of phase change materials: a review *Renew. Sustain. Energy Rev.* **158** 112172
[16] Dai Z, She X, Wang C, Ding Y, Zhang X and Zhao D 2023 Thermodynamic analysis on the performance of barocaloric refrigeration systems using neopentyl glycol as the refrigerant *J. Therm. Sci.* **32** 1063–73
[17] Aznar A, Lloveras P, Barrio M, Negrier P, Planes A, Mañosa L, Mathur N D, Moya X and Tamarit J-L-L 2020 Reversible and irreversible colossal barocaloric effects in plastic crystals *J. Mater. Chem.* A **8** 639–47
[18] Aznar A, Negrier P, Planes A, Mañosa L, Stern-Taulats E, Moya X, Barrio M, Tamarit J L and Lloveras P 2021 Reversible colossal barocaloric effects near room temperature in 1-X-Adamantane (X=Cl, Br) plastic crystals *Appl. Mater. Today* **23** 101023
[19] Li F, Li M, Niu C and Wang H 2022 Atomic-scale insights into the colossal barocaloric effects of neopentyl glycol plastic crystals *Appl. Phys. Lett.* **120** 073902
[20] Salvatori A, Negrier P, Aznar A, Barrio M, Tamarit J L and Lloveras P 2022 Colossal barocaloric effects in adamantane derivatives for thermal management *APL Mater.* **10** 111117
[21] Salvatori A *et al* 2023 Large barocaloric effects in two novel ferroelectric molecular plastic crystals *J. Mater. Chem.* A **11** 12140–50
[22] Meijer B E, Dixey R J C, Demmel F, Perry R, Walker H C and Phillips A E 2023 Dynamics in the ordered and disordered phases of barocaloric adamantane *Phys. Chem. Chem. Phys.* **25** 9282
[23] Murrill E and Breed L 1970 Solid-solid phase transitions determined by differential scanning calorimetry. Part I. Tetrahedral substances *Thermochim. Acta* **1** 239–46
[24] Font J, Muntasell J, Navarro J, Tamarit J L and Lloveras J 1987 Calorimetric study of the mixtures PE/NPG and PG/NPG *Sol. Energy Mater.* **15** 299–310
[25] Chandra D, Ding W, Lynch R A and Tomilinson J J 1991 Phase transitions in plastic crystals *J. Less-Common Met.* **168** 159–67
[26] Tamarit J L, Legendre B and Buisine J M 1994 Thermodynamic study of some neopentane derivated by thermobarometric analysis *Mol. Cryst. Liq. Cryst.* **250** 347–58
[27] Sun W and Ceder G 2017 Induction time of a polymorphic transformation *CrystEngComm* **19** 4576–85
[28] Serrano A, Duran M, Dauvergne J L, Doppiu S and Del Barrio E P 2021 Tailored transition temperature plastic crystals with enhanced thermal energy storage capacity *Sol. Energy Mater. Sol. Cells* **220** 110848
[29] Greer K F K and L A 2010 Heterogeneous nucleation *Pergamon Mater. Ser.* **15** 165–226
[30] Dai Z, Zhao D, She X, Zhang X, Shao B, Yin E and Ding Y 2022 Plastic crystal neopentyl glycol/multiwall carbon nanotubes composites for highly efficient barocaloric refrigeration system *SSRN Electron. J.* **32** 1–11
[31] Zhu L, Dai Z, Gao Y, Wu D, Wang C, Zhao D, She X, Ding Y and Zhang X 2023 Barocaloric material with high thermal conductivity for room-temperature refrigeration *J. Therm. Sci.* **32** 1–11
[32] Li F, Niu C, Xu X, Li M and Wang H 2022 The effect of defect and substitution on barocaloric performance of neopentylglycol plastic crystals *Appl. Phys. Lett.* **121** 223902